On line, real-time densimeter—Theory and optimization

Jin O. Kim and Haim H. Bau[a)]
Department of Mechanical Engineering and Applied Mechanics, University of Pennsylvania, Philadelphia, Pennsylvania 19104-6315

(Received 27 May 1988; accepted for publication 27 September 1988)

The speed of a torsional stress wave transmitted in a solid waveguide, which has a noncircular cross section and is submerged in a liquid, is inversely proportional to the density of the liquid. Thus, by measuring the speed of the torsional stress wave, information can be obtained about the density of the liquid or density-related characteristics such as liquid level and the mass composition of biphase mixtures. A predictive theory is developed to correlate the speed of the wave with the density of the liquid and the shape of the waveguide's cross section. The theory is used to optimize the waveguide's geometry so as to increase sensor sensitivity. The theoretical results are compared and found to favorably agree with experimental observations.

PACS numbers: 43.85.Dj, 43.88.Ct, 06.30.Dr

INTRODUCTION

The effect of adjacent fluid on the transmission of stress waves in solids may be utilized to measure various fluid characteristics. For example, since the speed of propagation of torsional stress waves in a rod with a noncircular cross section decreases as the density of the adjacent fluid increases, one can determine the density of the fluid by measuring the wave's speed of propagation. A device that operates on the aforementioned principle (hereafter referred to as the torsional wave sensor) can be installed permanently, in line, to monitor continuously density and density-related characteristics such as liquid level, composition of binary or biphase suspensions, etc.

Prototypes of torsional wave sensors have been manufactured by Lynnworth,[1] who also obtained a patent for the device.[2] These sensors have been used in experiments to measure fluid density,[3] liquid level,[4–7] void fraction of wet steam,[8] low gravity gauging of satellites' liquid propellant,[9] and aircrafts' residual fuel mass.

In a recent article, Bau[10] advanced a simple, approximate, predictive theory that provides a correlation between the speed of propagation of the torsional stress wave and the adjacent fluid density. The theoretically predicted results were found to be in good agreement with Lynnworth's[3] experimental observations. In this article, we shall use the aforementioned theory to optimize sensor sensitivity. We calculated the speed of the torsional stress wave in waveguides of different cross sections. Concurrently, we carried out a few experiments. The theoretical predictions were compared and found to favorably agree with the experimental observations.

I. THE APPARATUS

The apparatus consists of a waveguide, made of an elastic material of density ρ_s, with a uniform noncircular cross section, which is submerged in a liquid of density ρ_f and subjected to a torsional pulse (Fig. 1).

In our experiments, the torsional stress waves are conveniently introduced utilizing magnetostrictive phenomena. One end of a delay line made of a magnetostrictive material is soldered or glued to the waveguide. A coil is placed around the other end of the delay line (Fig. 1). The delay line is electrically polarized so as to develop a circumferential, permanent, magnetic field inside the magnetostrictive wire. The introduction of a current pulse into the coil causes a time varying axial magnetic field to develop. The interaction between the two aforementioned fields leads to a twisting force on the magnetostrictive wire and the generation of a torsional pulse. This is known as the Wiedemann effect.[11] The resulting torsional stress wave travels in the magnetostrictive wire. Part of the wave is reflected at the magnetostrictive wire–waveguide interface. The other part travels through the waveguide and is reflected from its other end. The reflected wave causes electromotive force in the coil, which now acts as a receiver. This is known as the inverse Wiedemann effect. The signal can be viewed on an oscilloscope's screen. In Fig. 2(a) and (b), we depict, respectively, typical signal traces from our experiments and the corresponding spectrum of the reflected wave. The signal denoted A in Fig. 2(a) is a result of the reflection from the delay line–waveguide interface, while the signal denoted B is a result of

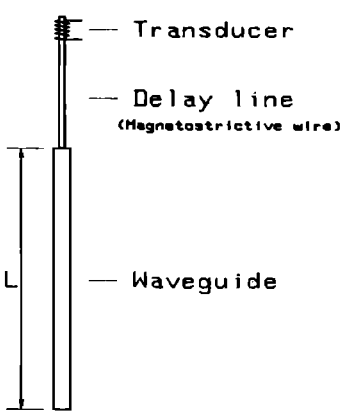

FIG. 1. Schematic description of the torsional wave sensor.

[a)] All correspondence should be addressed to this author.

 0001-4966/89/010432-08$00.80

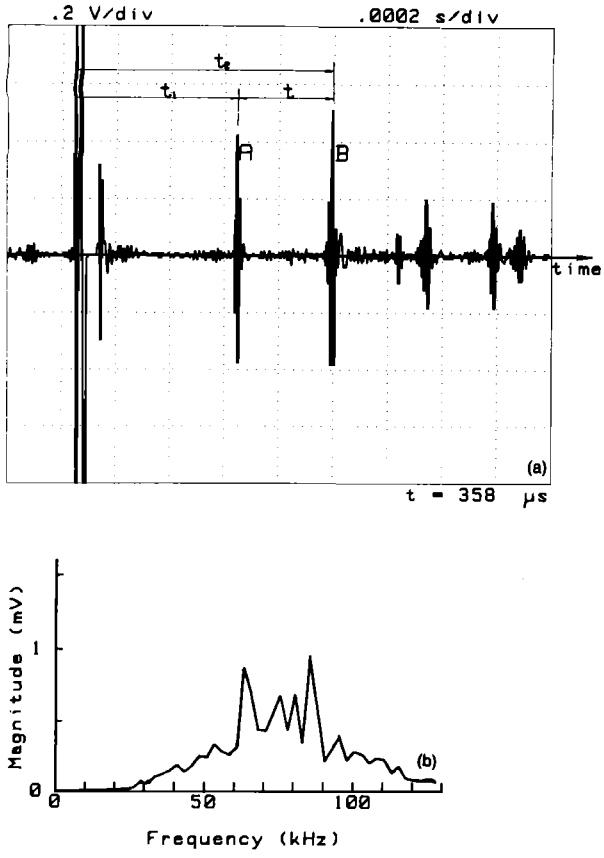

FIG. 2. (a) The signal trace of the reflected stress waves. (b) The spectrum of the reflected signal.

the reflection from the waveguide's end. By measuring the time ($t = t_2 - t_1$) that elapses between the two signals, one can calculate the speed of the torsional stress wave in a waveguide of known length (L). The time span is measured peak to peak. As we shall show later, this time span (or the wave speed) depends, among other things, on the densities of the waveguide and adjacent fluid and on the shape of the waveguide. From the spectrum depicted in Fig. 2(b), we conclude that the dominating frequencies are in the range of 60–90 kHz.

In our experiments, we typically employ waveguides made of stainless steel with length $L = 300$ mm. The delay line is made of "Remendur" (Co–Fe–V) of length about 1000 mm. The typical travel time of the torsional stress wave in a waveguide with a rectangular cross section (2.58 mm$\times$0.73 mm) in air is about 360 μs. The time span can typically be measured with a precision of 5 ns. The reflectivity of the delay line–waveguide interface can be controlled by adjusting the mechanical impedance mismatch at the interface. This is typically done by soldering a small ring around the waveguide.

The experimental procedure consists of either submerging the waveguide fully in liquids of various densities or varying the level of submersion of the waveguide in a given liquid. In the former case, the density of the adjacent liquid is correlated with the travel time of the torsional stress wave in the waveguide, while in the latter, the length of the wet portion of the waveguide is correlated with it.

II. THEORY

Consider a torsional stress wave traveling in a waveguide with a uniform, noncircular cross section submerged in a liquid. As the torsional wave travels through the waveguide, the solid–liquid interface is alternately accelerated and decelerated. Consequently, the inertia, which needs to be overcome by the torsion pulse, is a combination of the solid waveguide's inertia (I_s) and the adjacent liquid's apparent inertia (I_f). Thus, to the first-order approximation,[10] the torsional wave speed (c) can be calculated from the equation

$$c = K(G/\rho_s)^{1/2}(1 + \rho_f I_f/\rho_s I_s)^{-1/2}, \tag{1}$$

where G is the shear modulus of the solid, $K = (D/I_s)^{1/2} \leqslant 1$, and D is the torsional rigidity.

The fluid motion is induced by two mechanisms. The first mechanism is due to the existence of normal velocity component at the solid–fluid interface. This normal velocity component exists only when the solid's cross section is noncircular. This mechanism is active even when the fluid is inviscid. The second mechanism consists of viscous drag. The scale of the motion induced by the first mechanism is of the order of the size of the large dimension of the cross section [2(a)].Typically, a $\sim$0.003 m. The scale of the drag induced flow field is comparable to the thickness of the viscous boundary layer $(\nu T)^{1/2}$, where ν is the fluid's kinematic viscosity and T is the wave's period. For example, for a waveguide operating in water and glycerin at a frequency of 50 kHz and room temperature $a/(\nu T)^{1/2} \sim 10^3$ (water) and 30 (glycerin). Thus, in most circumstances, the fluid may be assumed inviscid. Consequently, I_f, as well as I_s and K, depends on the shape of the cross section alone.

In order to obtain the qualitative relationship between the wave speed (c) and the density ratio (ρ_f/ρ_s), one must obtain explicit expressions for K, I_s, and I_f. In this article, we describe first the technique used to calculate the apparent inertia of the fluid (I_f), and then the calculation of the torsional rigidity.

A. The apparent inertia of the fluid (I_f)

To obtain the apparent inertia of the fluid (I_f), one must calculate the flow field induced in the fluid by the torsional stress wave. We assume that the fluid is incompressible, inviscid, and at rest (except for the motion induced by the torsional stress wave). We also assume that the fluid motion is two dimensional.

We have ψ denote the stream function and B_1 and B_2 denote, respectively, the contour of the waveguide's cross section and some outer boundary (possibly at infinity). Here, R denotes the domain occupied by the fluid (Fig. 3). Thus we need to solve the boundary value problem[12]

$$\nabla^2\psi = 0 \quad \text{in } R \tag{2a}$$

$$\psi = \tfrac{1}{2}\omega \mathbf{r}^2 \quad \text{on } B_1, \tag{2b}$$

$$\psi = \text{const} \quad \text{on } B_2, \tag{2c}$$

and

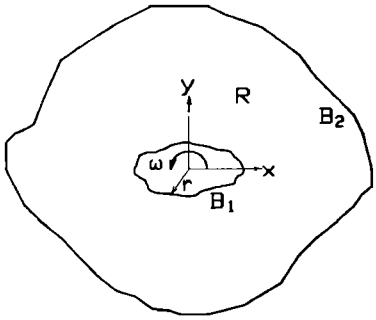

FIG. 3. The computational domain, where B_1 and B_2 are the sensor's surface and an external surface, respectively, and R is the domain occupied by the fluid.

$$\oint \frac{\partial \psi}{\partial n}\, ds = 0 \quad \text{on any closed contour surrounding } B_1. \tag{2d}$$

In Eq. (2), ∇^2 is the 2-D Laplacian, r is the distance from the center of rotation to a point on B_1, ω is the frequency of the torsional wave, $\partial/\partial n$ is a normal derivative (where n is normal to the contour), and ds is a length segment along the contour. Here, B_2 is an outer boundary located either at some finite distance from B_1 or at infinity.

Equations (2) can be solved analytically for simple cross sections such as the ellipse and the rectangle.[10] For more complicated cross sections, one must resort to numerical techniques.

Equations (2) are not convenient for direct numerical attack, since the explicit boundary condition on B_2 is not *a priori* known. To avoid the use of an iterative procedure, we separate the problem into two auxiliary problems and then use superposition.

The first auxiliary problem is

$$\begin{aligned} &\nabla^2 \psi_1 = 0, \quad @R, \\ &\psi_1 = \tfrac{1}{2}\omega r^2, \quad @B_1, \\ &\psi_1 = 0, \quad @B_2. \end{aligned} \tag{3}$$

The second is

$$\begin{aligned} &\nabla^2 \psi_2 = 0, \quad @R, \\ &\psi_2 = 0, \quad @B_1, \\ &\psi_2 = 1, \quad @B_2. \end{aligned} \tag{4}$$

The stream function for the original problem (2) is obtained by the superposition: $\psi = \psi_1 + \delta\psi_2$, where δ is some constant yet to be determined. It is easy to see that ψ satisfies the differential equation (2a), and the boundary conditions (2b) and (2c). The last condition (2d) requires

$$\delta = -\oint \frac{\partial \psi_1}{\partial n}\, ds \left(\oint \frac{\partial \psi_2}{\partial n}\, ds \right)^{-1}. \tag{5}$$

Thus, instead of having to solve the original boundary value problem (2), we can solve the two significantly simpler auxiliary problems, (3) and (4). Once the stream function ψ is calculated, the kinetic energy of the fluid $(\mathrm{KE})_f$ per unit length of the waveguide can be computed in a straightforward way, i.e.,

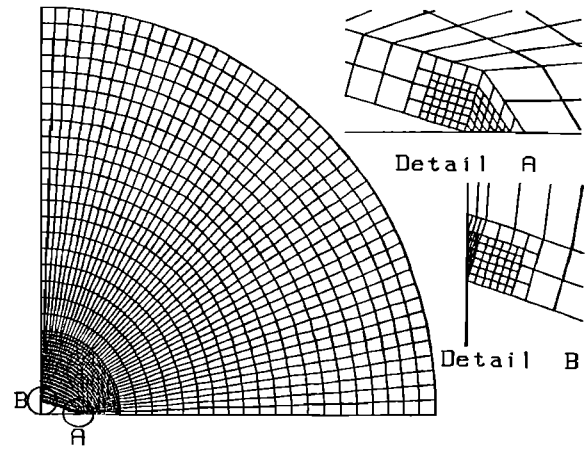

FIG. 4. The finite element mesh used in the computation of the flow field around a diamond-shaped cross section.

$$(\mathrm{KE})_f = \frac{1}{2}\rho_f \int\int_R \nabla\psi \cdot \nabla\psi\, dA = \frac{1}{2}\rho_f \int_{B_1} \psi \frac{\partial \psi}{\partial n}\, ds. \tag{6}$$

Typically, we prefer to use the area integral in (6), rather than the line integral, in order to minimize possible inaccuracies that may occur as a result of corner singularities. Since the velocity of the solid–liquid interface is relatively small, there is no need to include energy losses due to acoustic radiation.[13]

The apparent inertia (I_f) is obtained from

$$I_f = (\mathrm{KE})_f / \tfrac{1}{2}\rho_f \omega^2. \tag{7}$$

Equations (3) and (4) are solved using finite elements. The finite element mesh for a diamond-shaped cross section is depicted, as an example, in Fig. 4. Since the flow field possesses double symmetry, only one quarter of the domain needs to be considered. We use rectangular elements whose size varies gradually. Since most of the fluid motion occurs next to the internal boundary, we employ fine mesh there. As the distance from the waveguide increases, we use progressively coarser meshes. To counteract the adverse effect of corner singularities on the accuracy of the numerical results, we concentrate a larger number of elements in the vicinity of the corners. See details A and B in Fig. 4. To verify the numerical code, we compare the computational results for a rectangular cross section with the analytical ones.[10] The agreement is always better than 1.5%.[14]

The numerical solution has to be carried out on a finite domain R. We test the effect of the location of the outer boundary (B_2) on the magnitude of the apparent inertia (I_f) and determine that, unless B_2 is very close to B_1 (i.e., within a distance on the order of the scale of the edge of the cross section), the apparent inertia of the fluid (I_f) is not affected significantly by the location of B_2 (see the Appendix for more details). Thus, in our calculations of the apparent inertia of an externally unbounded fluid, we assume that the boundary B_2 is located about ten edge sizes from the center of rotation (Fig. 4).

The flow field around the diamond-shaped cross section is depicted, for example, in Fig. 5, where we depict the equal-

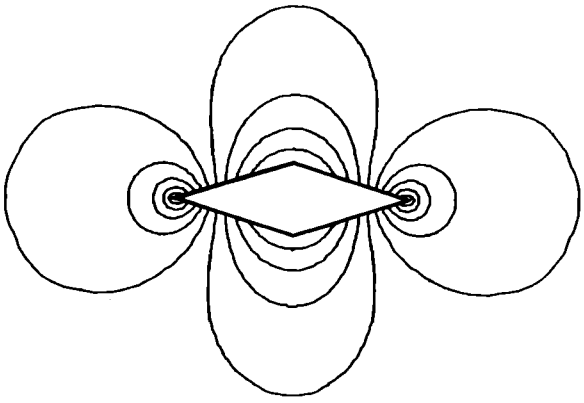

FIG. 5. The flow field (streamlines) induced by a diamond-shaped cross section of aspect ratio 3.3.

ly spaced streamlines. Since the flow is time dependent, the streamlines do not trace the actual path of any fluid particle. The velocity vector of the fluid particles is tangent to the streamlines.

The results of our computations are summarized in Fig. 6, where we depict in solid lines the ratio I_f/I_s as a function of the aspect ratio (a/b) for the diamond-shaped, elliptical, rectangular, and cross-shaped cross sections. The dashed line represents theoretical data obtained for two (nonsimilar) hexagonal cross sections, which we used in some of our experiments. The circles in Fig. 6 correspond to experimental results obtained for hexagonal and rectangular waveguides fully submerged in water. The theoretical and experimental results will be compared in more detail later on in the article. Note that the ratio I_f/I_s represents the sensor's sensitivity. The theory predicts an improvement in sensitivity as the solid's inertia is reduced. This trend has been verified experimentally for solid cross sections but not for hollow ones.

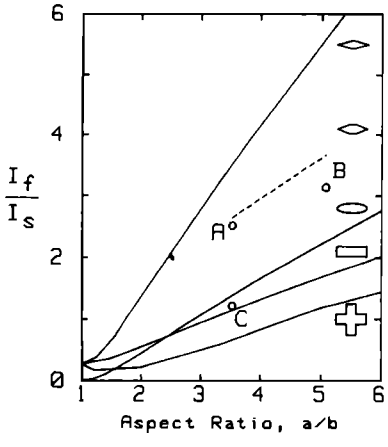

FIG. 6. The apparent inertia (I_f/I_s) of the diamond-shaped, elliptical, rectangular, and cross-shaped cross sections depicted as a function of the aspect ratio a/b. The solid lines and the symbols correspond to theoretical and experimental results, respectively. The experimental results are for hexagonal cross sections of aspect ratios 3.5(A) and 5(B), and a rectangular cross section of aspect ratio 3.5(C).

B. Torsional rigidity

In order to calculate the torsional wave speed [Eq. (1)], we also need to know the torsional rigidity of the waveguide. To this end, we employ the standard torsion theory of thin rods.[15] Briefly, we assume that when the torsional stress pulse is applied to the waveguide, neighboring cross sections at distance dz apart rotate through relative angle $d\phi$, which is assumed small. We define the stress function $H(x, y)$ in such a way that the shear stresses (τ) in the x and y directions are given by

$$\tau_{zx} = G\frac{d\phi}{dz}\frac{\partial H}{\partial y}, \quad \tau_{zy} = -G\frac{d\phi}{dz}\frac{\partial H}{\partial x}, \tag{8}$$

where (x, y) are Cartesian coordinates lying in the cross section's plane (Fig. 3).

The equilibrium condition suggests that the stress function should satisfy Poisson's equation[15]

$$\nabla^2 H = -2, \tag{9}$$

while the requirement that the lateral surface of the rod will be stress free leads to the boundary condition

$$H = \text{constant}, \quad @B_1, \tag{10}$$

where B_1 is the boundary of the cross section (Fig. 3).

We note in passing that the boundary condition (10) ignores the interaction between the pressure field in the adjacent fluid and the stress field in the solid. Thus the above boundary condition is not strictly correct, and it may serve only as a first-order approximation.

We solve Eqs. (9) and (10) analytically for simple cross sections, such as the ellipse and the rectangle, and numerically using finite elements for the more complicated cross sections considered in this article. The numerical technique is validated by comparing its predictions for the rectangular cross section with analytical results. The agreement is better than 1.5%. Once the stress function $H(x, y)$ is known, the torsional rigidity (D) can be calculated from the area integral[15]

$$D = 2\int\int H(x, y)dx\,dy. \tag{11}$$

In Fig. 7, we plot in solid lines the calculated values of

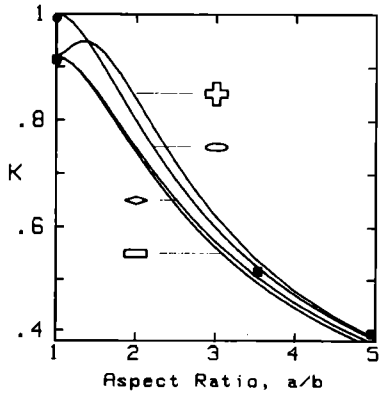

FIG. 7. The ratio between the speed of a torsional wave in rectangular, diamond-shaped, elliptical, and cross-shaped cross sections and a corresponding circular cross section is depicted as a function of the aspect ratio (a/b).

$K = (D/I_s)^{1/2}$ as a function of the aspect ratio for the ellipse, rectangle, diamond, and cross-shaped cross sections. The symbols correspond to experimental observations for the circular and rectangular cross sections. We note that the agreement between experiment and theory deteriorates as the aspect ratio increases. This deterioration is attributed to dispersion effects, which were excluded for the simple theory.

Physically, K represents the ratio between the speed of the torsional stress wave in each of the above cross sections and a corresponding circular cross section of radius a.

III. COMPARISON WITH EXPERIMENTS

In order to verify the theoretical predictions described in Sec. II., we carried out a few experiments. The experimental observations consisted of measuring the flight time (t) of the torsional stress wave in the waveguide (see Fig. 2). We denote by t_0 the transmission time for a waveguide in air. This quantity (t_0) is taken as an approximation for the flight time in a waveguide in vacuum. Here, $Dt = t - t_0$ denotes the difference in the transmission time of a wave in a waveguide submerged in liquid and one in vacuum.

For a waveguide fully submerged in liquid, Eq. (1) suggests

$$\frac{Dt}{t_0} = \left(1 + \frac{\rho_f I_f}{\rho_s I_s}\right)^{1/2} - 1 \approx \frac{1}{2}\frac{\rho_f I_f}{\rho_s I_s}, \tag{12}$$

where the approximation is valid for $\rho_f I_f/\rho_s I_s \ll 1$. We measured Dt for waveguides with rectangular and hexagonal cross sections fully submerged in water. The ratio I_f/I_s was calculated from Eq. (12) and depicted in Fig. 6 for a rectangular cross section of aspect ratio 3.5 and hexagonal cross sections of aspect ratios 3.5 and 5. For both geometries with an aspect ratio of 3.5, excellent agreement (about 1%) was obtained between the theoretically predicted and the experimentally observed results. For aspect ratio 5, the discrepancy between experiment and theory was about 10%. This discrepancy is attributed to dispersion effects, which we discuss later.

Next, we partially submerged the waveguides in water. The wet portion of the waveguide's length is denoted as l while the full length is L. The flight time Dt can be theoretically correlated with the wet portion of the length as follows:

$$\frac{Dt}{t_0} = \frac{l}{L}\left[\left(1 + \frac{\rho_f I_f}{\rho_s I_s}\right)^{1/2} - 1\right] \sim \frac{1}{2}\frac{l}{L}\frac{\rho_f I_f}{\rho_s I_s}, \tag{13}$$

where the approximation is valid for $\rho_f I_f/\rho_s I_s \ll 1$.

Figure 8 depicts the ratio Dt/t_0 as a function of the normalized wet length portion (l/L) for the following: (a) hexagonal cross section of aspect ratio 5; (b) hexagonal cross section of aspect ratio 3.5; (c) rectangular cross section of aspect ratio 3.5; (d) solid square; and (e) hollow square. The solid lines and symbols represent theoretical and experimental results, respectively. The solid (hollow) circles correspond to solid (hollow) cross sections. For the solid cross sections of aspect ratio 3.5 and smaller, we find excellent agreement (within 4%) between the experimental observations and theoretical predictions. For the large aspect ratio cross sections ($a/b \cong 5$), the deviation between theory and experiment is about 10%. This is consistent with the results depicted in Fig. 6, and it is attributed to dispersive effects that are absent in the simple theory. For the hollow cross section, there is poor agreement between theory and experiment. The hollow cross section does not live up to its promise and does not significantly outperform its solid counterpart.

Next, we examine the effects of density variations on the flight time. We submerged fully the waveguide in a solution of calcium chloride in water. The density of the solution was varied by changing the salt concentration. In Fig. 9, we depict Dt/t_0 as a function of the relative density. The solid lines and symbols represent theoretical and experimental results for the rectangular and hexagonal cross sections. The scatter of the experimental data Dt/t_0 was smaller than 0.2% and 0.15% for the rectangular and hexagonal cross sections. The deviation between the experimental data and the theoretical

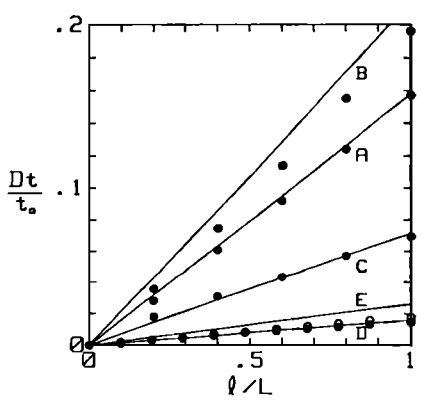

FIG. 8. The ratio Dt/t_0 is depicted as a function of the wet length l/L for (A) a hexagonal cross section ($a/b = 3.5$); (B) a hexagonal cross section ($a/b = 5$); (C) a rectangle cross section ($a/b = 3.5$); (D) a solid square cross section; and (E) a hollow square with wall thickness ratio 0:288. The solid lines and symbols corespond to theoretical and experimental results, respectively. The solid (hollow) circles correspond to solid (hollow) waveguides.

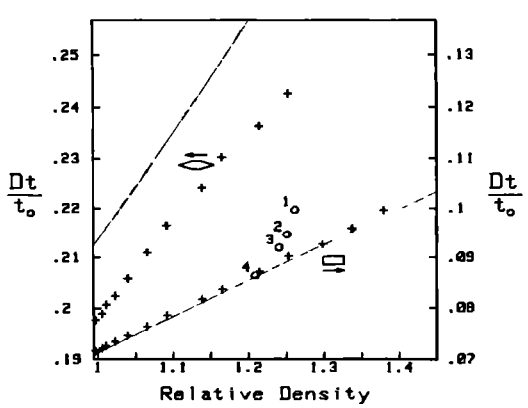

FIG. 9. The ratio Dt/t_0 is depicted as a function of the relative density of a salute solution. The solid lines and the symbols represent theoretical and experimental results, respectively. The crosses and circles correspond to experiments conducted in calcium chloride solution in water and a glycercin–water solution, respectively.

curve for the hexagonal cross section is attributed to dispersion effects. Figure 9 gives some indication about the kind of resolution one may expect to obtain from this device. In Fig. 9, we also examine briefly the effects of viscosity on the waveguide's performance when the rectangular waveguide is submerged in liquids of various viscosities. The points denoted 1, 2, 3, and 4 in Fig. 9 correspond to liquids with viscosities $\nu \sim 1180$, 620, 310, and 50×10^{-6} m^2/s. The viscosity of water at room temperature is about 10^{-6} m^2/s. We note in passing that viscous effects become significant only when $2a/\sqrt{\nu T} < 100$, where $2a$ represents the larger dimension of the cross section.

In summary, the simple theory presented in Sec. III agrees favorably with experimental observations for solid cross sections with small to moderate aspect ratios (i.e., up to $a/b \sim 3.5$). As the aspect ratio increases, the deviation between the theoretical and experimental results increases as well. This increasing discrepancy is attributable to the rise in dispersive effects as the aspect ratio is increased. Dispersive phenomena were excluded from our simple theory (Sec. II).

To be more specific, dispersion's importance increases as the ratio of the cross section's large dimension ($2a$) and the wavelength (λ) increases. We estimate the length of the stress wave $\lambda \approx 30$–50 mm. The typical larger dimension ($2a$) of the cross section is 2.6 and 6.1 mm for $a/b = 3.5$ and 5. Thus $2a/\lambda \sim 0.06$ and 0.15 for $a/b = 3.5$ and 5. Therefore, dispersion phenomena are much more important in the case of the wider cross sections.

The theory also failed to predict the correct wave speed in the square waveguide with the square hole. We speculate that in the case of the thin wall tube, warping effects cannot be neglected. It is also possible that in the case of the hollow tube, other types of stress waves are induced in addition to the torsional ones. These additional effects were excluded from our simple theory (Sec. II).

IV. SENSOR OPTIMIZATION

The analysis of Sec. II suggests that sensor sensitivity is directly proportional to the ratio I_f/I_s. Since the ratio I_f/I_s clearly increases monotonically as the aspect ratio (a/b) increases, it would seem desirable to operate with as large an aspect ratio as possible (see Fig. 6). Unfortunately, the aspect ratio cannot be increased without limit. A minimum value must be set for b to assure structural integrity. Additionally, the value of a should be well below the wavelength of the torsional stress wave so as to minimize dispersion.

For a fixed ratio, the I_f/I_s ratio may be increased by a proper choice of geometrical configurations for the cross section. For example, for aspect ratio $a/b = 5$, the diamond-shaped cross section is 3.3 times more sensitive than the rectangular cross section (Fig. 6). Below, we shall set forth physical arguments for the diamond-shaped cross section outperforming the elliptical one, and the elliptical one outperforming the rectangular cross section.

The fluid's apparent inertia (I_f) around the rectangle exceeds that around the ellipse and the diamond. However, as the aspect ratio increases, all these apparent inertias approach the common limit $I_f = 1/8\ \pi a^4$, which is the apparent inertia of the flat plate of length $2a$ rotating about its center. In the case of the diamond and that of the ellipse, the limit is approached from below, while in the case of the rectangle, the limit is approached from above. The same is not true, however, with regard to the cross section's polar moment of inertia (I_s). The moments of inertia (I_s) do not approach a common limit as a/b increases. For example, in the cases of the ellipse and the rectangle, the ratio of the polar moments of inertia is fixed and equals $16/(3\pi)$.

The foregoing suggests a clear means of improving the sensor's sensitivity. One ought to reduce the cross section's polar moment of inertia (I_s) as much as possible. The diamond-shaped cross section has a lower polar moment of inertia than the rectangular cross section does. We conceivably could further improve upon the diamond-shaped cross section by using concave curves rather than the diamond's straight lines.

One might be tempted to try to increase the fluid's apparent inertia (I_f) by using a winged (or finned) cross section. One example of the winged cross section is the cross shape. Figure 6 suggests, however, that the performance of the cross-shaped cross section is worse than that of the other cross sections considered. In what follows, we shall try to explain why this is the case. In order to simplify the mathematical treatment, we consider a winged cross section with N fins of zero thickness (Fig. 10). In Fig. 10, $N = 8$. The cross-shaped cross section corresponds to $N = 4$. The fluid's apparent inertia can be calculated from the expression[16]:

$$I_f = \frac{1}{2} a^4 \left(\frac{\Gamma(2/N + \frac{1}{2})}{\Gamma(2/N + 1)} \right)^2, \tag{14}$$

where Γ is the gamma function. For $N = 1$ and $N = 2$, the expression (14) reproduces the classical results for a flat plate in rotation about one of its ends and its center, respectively.

The first four values and the asymptotic value as $N \to \infty$ for I_f/a^4 are given in Table I. Note that as N increases, the apparent inertia increases at a rate less than a linear function of N. In other words, doubling the number of wings (or fins) does not double the apparent inertia. At the same time, if the fins were of finite thickness (as they would be in any practi-

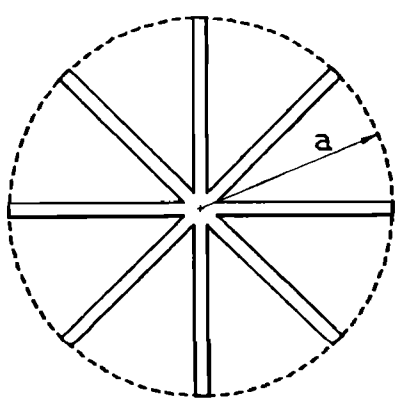

FIG. 10. A winged cross section with N zero-thickness fins ($N = 8$ in the figure).

TABLE I. Apparent inertia of a finned cross section as a function of the number of fins.

N	I_f/a^4
1	0.221
2	0.393
3	0.528
4	0.637
⋮	⋮
∞	1.57

cal case), the polar moment of inertia will increase almost linearly with the number of fins. Consequently, as the number of fins increases, the ratio I_f/I_s will decrease.

Likewise, the cross-shaped cross section we dealt with in Fig. 6 does, in fact, induce a higher apparent inertia (I_f) than any of the other cross sections in Fig. 6, but, at the same time, the polar moment of inertia (I_s) increased even faster. Thus, on balance, the performance of the cross-shaped cross section was worse than that of the other cross sections depicted in Fig. 6. In sum, winged (or finned) cross sections are likely to reduce the ratio (I_f/I_s) and thus are not desirable for our purposes.

Another conceivable means of reducing the waveguide's polar moment of inertia is the deployment of hollow waveguides. Unfortunately, our experiments with the square waveguide with a square bore suggest that the use of hollow waveguides will not always contribute to the sensor's sensitivity because of the excitation of stress waves other than the torsional ones. It is possible, however, that better results than those reported here would be obtained using hollow waveguides with special shaped bores such as those bounded by a stress line.[15]

Sensor sensitivity, conceivably, also might be improved by increasing the apparent inertia of the fluid (I_f) by externally confining the fluid, i.e., by placing the waveguide inside a tube. Indeed, it may be desired to use such an external tube to provide a mechanical protection for the waveguide. However, for such a confinement to yield a significant increase in the fluid's apparent inertia, a very narrow gap between the waveguide and the confinement must be maintained (see the Appendix). Such a narrow gap probably would not be acceptable in many applications.

V. CONCLUSIONS

A simple theory has been advanced to predict the performance of a torsional wave sensor. The theory is applicable for waveguides with solid cross sections whose larger dimension is smaller than 0.1 of the wavelength. The theoretical predictions have been compared and found to favorably agree with experimental observations.

The theory was used to optimize sensor performance. To improve the sensor sensitivity, one must maximize the ratio I_f/I_s and minimize the density of the waveguide (ρ_s). The ratio (I_f/I_s) increases monotonically as the aspect ratio (a/b) increases. However, for practical reasons, the aspect ratio a/b cannot be increased without limit. A minimum value must be set for b to assure structural integrity, and the value of a should be well below the length of the torsional wave in order to minimize dispersion. For a fixed aspect ratio, it appears that the diamond-shaped cross section outperforms the other cross sections considered in this paper (rectangular, elliptic, cross-shaped, and winged).

ACKNOWLEDGMENTS

This work has been supported by the National Science Foundation (Grant CBT 8351658), the Electric Power Research Institute (RP 2515-03), and Panametrics. We gratefully acknowledge useful discussions and encouragement from L. C. Lynnworth of Panametrics.

APPENDIX: EFFECTS OF CONFINEMENT ON SENSOR PERFORMANCE

In this appendix, we consider how the presence of external physical constraints, such as those imposed by a casing designed to protect the sensor from mechanical damage, may affect the performance of the torsional wave sensor. We shall also demonstrate that external confinement may be used to increase the sensor's sensitivity.

For demonstration purposes, we carry out the calculations for a sensor with an elliptical cross section and an external boundary composed of a confocal ellipse (Fig. A1). In essence, we need to solve Eq. (2). The geometrical configuration in this particular case suggests the use of an elliptical coordinate system. We denote the elliptical coordinates (ξ, β). The relationship between the Cartesian (x,y) and the elliptical coordinates (ξ, β) is given by the expressions:

$$x = c \cosh \xi \cos \beta,$$
$$y = c \sinh \xi \sin \beta, \tag{A1}$$

where ξ_1, and ξ_2 describe the inner and outer ellipses, respectively. The relationship between the semiaxes and ξ_i is given by

$$a_i = c \cosh \xi_i, \quad b_i = c \sinh \xi_i,$$
$$c^2 = a_i^2 - b_i^2, \quad i = 1,2. \tag{A2}$$

The solution for the flow field (streamfunction) can readily be obtained in the form:

$$\psi = \frac{1}{4}\omega c^2 \left(\cosh 2\xi_1 + \frac{\sinh[2(\xi_2 - \xi)]}{\sinh[2(\xi_2 - \xi_1)]} \cos 2\beta \right). \tag{A3}$$

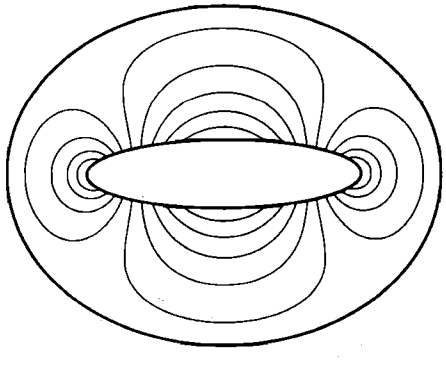

FIG. A1. The flow field (streamlines) between two confocal ellipses of aspect ratio $a/b = 4$ and axes' ratio $b_2/b_1 = 5$.

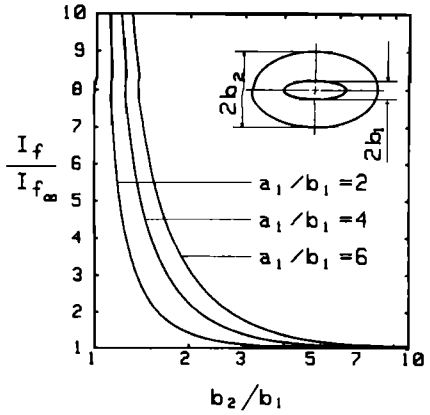

FIG. A2. The ratio I_f/I_{f_∞} depicted as a function of the axes' ratio b_2/b_1. Here, I_f and I_{f_∞} are the apparent inertia for the confined and unconfined ellipse, respectively.

The contours of the constant value stream functions are shown in Fig. A1. The fluid's apparent inertia (I_f) can be expressed as follows:

$$I_f = (\pi c^4/8)\coth 2(\xi_2 - \xi_1)$$
$$= \frac{\pi c^4}{16}\frac{(a_1^2 + b_1^2)(a_2^2 + b_2^2) - 4a_1a_2b_1b_2}{a_2b_2(a_1^2 + b_1^2) - a_1b_1(a_2^2 + b_2^2)}. \quad \text{(A4)}$$

In contrast, the apparent inertia of the unbounded fluid (I_{f_∞}) is

$$I_{f_\infty} = \pi c^4/8. \quad \text{(A5)}$$

That is, $I_f/I_{f_\infty} > 1$.

In Fig. A2, we depict the ratio I_f/I_{f_∞} as a function of b_2/b_1, which represents the relative gap thickness between the inner and outer boundaries. Two important conclusions can be drawn from Fig. A2. First of all, for cases of $b_2/b_1 > 4$, the fluid's apparent inertia may be taken as that of an unbounded fluid for any practical purpose. Second of all, one can increase the fluid's apparent inertia, and thus sensor sensitivity, by confining the torsional wave sensor in an external casing. The smaller the gap between the sensor and its casing, the higher the sensitivity is. Of course, the smallest feasible magnitude of the gap will be dictated by the environment in which the sensor is operating. The cleaner the environment, the smaller the gap may be.

[1]L. C. Lynnworth, "New Designs for Magnetostrictive Probes Using Extensional, Torsional and Flexural Waves," in *Ultrasonics Symposium Proceedings* (IEEE, New York, 1978), pp. 300–304.

[2]L. C. Lynnworth, U. S. Patent 4,193,291, "Slow Torsional Wave Densimeter" (1980).

[3]L. C. Lynnworth, "Slow Torsional Wave Sensors," in *Ultrasonics Symposium Proceedings* (IEEE, New York, 1977), pp. 29–34.

[4]G. N. Miller, R. L. Anderson, S. C. Rogers, L. C. Lynnworth, W. B. Studley, and W. R. Wade, "High Temperature, High Pressure Water Level Sensor," in *Ultrasonics Symposium Proceedings* (IEEE, New York, 1980), pp. 877–881.

[5]W. B. Dress, "A High Resolution Ultrasonic Densitometer," in *Ultrasonics Symposium Proceedings* (IEEE, New York, 1983), pp. 287–290.

[6]W. B. Dress and G. N. Miller, "An Ultrasonic Level and Temperature Sensor for Power Reactor Applications," in *1st Proceedings of Nuclear Thermal Hydraulics Winter Meeting* (ANS, New York, 1983), pp. 240–247.

[7]J. F. Kirkpatrick and W. C.Kuzniak, "Development of Large-Scale Acoustic Waveguides for Liquid-Level Measurements," Trans. Am. Nucl. Soc. **55**, 719–721 (1987).

[8]A. Arave, E. Fickas, and W. A. Shurtliff, "Ultrasonic Density Detector for In-core Dynamic Measurements," Instrum. Aerosp. Ind. **24**, 609–620 (1978).

[9]S. A. Jacobson, J. M. Korba, L. C. Lynnworth, T. H. Nguyen, G. F. Orton, and A. J. Orazietti, "Low-Gravity Sensing of Liquid/Vapor Interface and Transient Liquid Flow," IEEE Trans. Ultrason., Ferroelec. Freq. Control **UFFC-34**, 212–224 (1987).

[10]H. H. Bau, "Torsional Wave Sensor—A Theory," Trans. ASME, J. Appl. Mech. **53**, 846–848 (1986).

[11]N. S. Tzannes, "Joule and Wiedemann Effects—The Simultaneous Generation of Longitudinal and Torsional Stress Pulses in Magnetostrictive Materials," IEEE Trans. Sonics Ultrason. **SU-13**(2), 33–41 (1966).

[12]H. Lamb, *Hydrodynamics* (Dover, New York, 1945), 6th ed., pp. 86–87.

[13]P. M. Morse and K. U. Ingard, *Theoretical Acoustics* (McGraw-Hill, New York, 1968), Chap. 7.

[14]J. O. Kim, "The Interaction between Stress Waves Transmitted in Solid Waveguides and Adjacent Medium," Ph.D. thesis, University of Pennsylvania (1989).

[15]I. S. Sokolnikoff, *Mathematical Theory of Elasticity* (McGraw-Hill, New York, 1956), pp. 114–119, pp. 169–177.

[16]J. N. Newman, "Added Moment of Inertia of Two-Dimensional Cylinders," J. Ship Res. **23**, 1–8 (1979).